AIMS Materials Science, 13(5): 996–1016.
DOI: 10.3934/matersci.2026047
Received: 25 August 2026
Revised: 12 October 2026
Accepted: 28 October 2026
Published: 10 November 2026

https://www.aimspress.com/journal/Materials

Research article

Finite-element-informed CNN–LSTM and cellular automata prediction of microstructure evolution in QP1180 steel laser welding

Xiaojuan Li[1,2], Zhenfei Zhan[1,*], Liangjun Zhang[2], Silong Zhou[2], Zhong Liao[2], Huayang Xiang[1], Yuxiang Ji[3] and Fuhao Fan[1,2]

[1] College of Mechanical and Electrical Engineering & Vehicle Engineering, Chongqing Jiaotong University, No. 66 Xuefu Avenue, Nan'an District, Chongqing 400074, China
[2] Chongqing Wanfeng Aowei Aluminum Wheel Co., Ltd., No. 88 Jiade Avenue, Caijiagang Town, Beibei District, Chongqing 400700, China
[3] Design School, Xi'an Jiaotong-Liverpool University, 111 Ren'ai Road, Suzhou Industrial Park, Suzhou, Jiangsu 215123, China

* **Correspondence:** Email: 622240790049@mails.cqjtu.edu.cn; Tel: +86-139-0948-8330; Fax: +86-23-62652644.

Abstract: Rapid thermal cycling during laser welding strongly affects the microstructure of advanced high-strength steels, whereas repeated finite-element simulations across process conditions are computationally expensive. In this study, we developed a finite-element-informed convolutional neural network–long short-term memory (CNN–LSTM) and a two-dimensional cellular automaton (CA) framework for cooling-rate prediction and assessment of solidification-grain morphology in laser-welded QP1180 steel. A three-dimensional thermophysical finite element (FE) model was calibrated against a local thermocouple temperature history. At the calibration location, the selected peak-temperature and cooling-rate differences were below 5% and 10%, respectively. The calibrated model was then used to generate cooling-rate fields for 300 combinations of laser power, welding speed and defocusing distance obtained by Latin hypercube sampling. The CNN–LSTM surrogate mapped the three process parameters to a 200-dimensional cooling-rate field extracted from a 10 × 20 grid. On the fixed held-out test set, the model achieved a coefficient of determination (R^2) of 0.88, a mean absolute error (MAE) of 0.25, and a root mean square error (RMSE) of 0.38. It yielded a higher R^2 and lower MAE and RMSE than the standalone CNN and LSTM models. The predicted cooling-rate fields were converted into approximate local temperature histories over the solidification interval and coupled with the CA model. The simulated morphology reproduced the qualitative transition from columnar grains near the

fusion boundary to a more equiaxed region toward the weld center. The framework was restricted to the investigated QP1180 lap-joint configuration and process window. The CA output represented solidification-grain morphology rather than the final multiphase microstructure; quantitative grain-scale validation and broader extrapolation require further experimental evidence.

Keywords: QP1180 steel; laser welding; finite element simulation; CNN–LSTM; cellular automata; microstructure evolution; cooling-rate prediction

1. Introduction

Advanced high-strength steels (AHSSs) are widely used in lightweight automotive structures because they combine high strength with reduced sheet thickness. Studies on laser-welded QP980 steel have examined the fusion-zone microstructure, heat-affected zone (HAZ) characteristics, and tensile behavior [1,2]. Related investigations of quenching and partitioning steels have also explored weld morphology, microstructure evolution, and mechanical performance under different laser-welding conditions [3–5]. Accurate prediction of the thermal history and resulting microstructure is therefore essential for assessing weld morphology and selecting suitable process conditions.

Physics-based models are widely used to predict laser-induced thermal fields and solidification microstructures. Finite-element (FE) and finite-volume (FV) methods can resolve transient heat transfer, molten-pool evolution, and cooling-rate distributions generated by a moving heat source [6,7]. The resulting thermal variables provide the boundary conditions required to model phase transformation and grain growth. Phase-field, Monte Carlo, and cellular automata (CA) methods have therefore been coupled with calculated thermal fields to describe nucleation, competitive grain growth, solute redistribution, and the columnar-to-equiaxed transition during rapid solidification. Reviews of mechanistic modeling in metal additive manufacturing have emphasized that process–structure–property predictions require experimentally calibrated thermal models because errors in the calculated temperature field propagate into the predicted microstructure and properties. Although many of these modeling advances have been developed for laser additive manufacturing, laser welding involves similar thermal physics: a moving, localized heat source generates steep temperature gradients, high cooling rates, and rapid solidification that govern the resulting weld structure.

Coupled thermal–microstructural models are widely used to predict grain morphology in laser-based manufacturing. Zhang et al. coupled FE thermal simulations with a CA model to predict the thermal history and grain morphology of Ti-6Al-4V during direct metal deposition [8]. Lian et al. developed a CA–FV method for simulating microstructure evolution during additive manufacturing and demonstrated the importance of accurate molten-pool temperature fields for grain-scale predictions [9]. Subsequent researchers have sought to improve the computational efficiency and spatial resolution of these models. Teferra and Rowenhorst optimized a CA–FE framework to simulate large microstructural domains [10], whereas Liu and Shin combined CA and phase-field (PF) models to describe solidification and solute evolution in Ti-6Al-4V [11]. Collectively, these studies show that CA-based models can predict physically meaningful grain morphologies, but their reliability depends on accurate, spatially resolved thermal histories [12–14].

Despite these advances, repeated high-fidelity thermal simulations remain computationally expensive for rapid evaluation of multiple process conditions. A calibrated FE model can analyze

individual welding cases but becomes inefficient when laser power, welding speed, and defocusing distance are varied across a broad process window. Surrogate models and physics-informed machine learning have therefore been introduced to reduce the computational cost of laser-based manufacturing simulations [15,16]. Ren et al. developed a physics-based machine-learning method for predicting thermal fields along laser-scanning paths, reducing the cost of evaluating different scanning strategies. Gunasegaram et al. highlighted the importance of multiscale, multiphysics models and computationally efficient surrogates for digital twins of metal additive manufacturing [17,18]. Moreover, Tang et al. integrated physics-informed neural networks with a CA model to calibrate thermo-microstructural simulations of laser powder-bed fusion [19–21]. However, most learning-assisted studies have focused on temperature-field reconstruction, molten-pool geometry, or process monitoring. Relatively few researchers have linked predicted cooling-rate fields to grain-scale microstructure evolution and experimental metallographic observations.

A further challenge is that purely data-driven models do not explain the physical origin of the predicted weld structure. For laser-welded QP1180 steel, the relevant prediction target extends beyond the thermal field to the grain morphology established during solidification. The principal features include columnar growth near the fusion boundary, a more equiaxed morphology toward the weld center, and the transition between these regions. Moreover, thermo-microstructural studies suggest that combining rapid field prediction with CA-based solidification modeling can improve the physical interpretability of microstructure predictions. However, this integrated approach remains insufficiently explored for QP1180 steel laser welding, particularly for connecting process parameters and cooling-rate fields to experimentally observed grain-morphology trends.

In this study, we develop an FE-informed convolutional neural network–long short-term memory (CNN–LSTM) and CA framework for predicting solidification-grain morphology in laser-welded QP1180 steel. Laser-welding experiments and metallographic characterization provide the experimental basis for model calibration and morphology-level assessment. A calibrated three-dimensional thermophysical FE model generates cooling-rate fields across a process window sampled by Latin hypercube sampling. The CNN–LSTM surrogate then maps the welding parameters to the spatial cooling-rate field, which is converted into local solidification temperature histories and supplied to the CA model. The simulated morphology is compared with metallographic observations to assess whether the coupled framework reproduces the principal transition from columnar grains near the fusion boundary to a more equiaxed region toward the weld center.

The methodological contribution lies in the integration of an FE-derived thermal dataset, a spatial cooling-rate-field surrogate, and a CA solidification model. The calibrated FE model first provides physically based cooling-rate fields for surrogate training, reducing the need to repeat the complete FE analysis for every candidate condition within the investigated domain. The surrogate output is then converted into local temperature histories over the solidification interval, thereby preserving a physical connection between the process parameters and the thermal input to the CA model. Finally, the framework is applied to QP1180 lap-joint laser welding and assessed against the experimentally observed columnar-to-equiaxed morphology trend. This approach differs from conventional CA–FE calculations performed independently for each condition and from learning-assisted thermal predictions that are not coupled to grain-scale solidification modeling.

2. Materials and methods

2.1. Materials and experimental procedures

QP1180 steel sheets with a thickness of 1.2 mm were used as the base material. The nominal chemical composition is listed in Table 1. Two sheets, each measuring 100 × 100 × 1.2 mm, were assembled in a lap configuration with an overlap length of 15 mm. Figure 1 shows the geometry and dimensions of the laser-welded lap-joint specimen.

Table 1. Chemical composition of the QP1180 steel (wt.%).

Element	Mn	Si	C	Al	Cu	Nb	Ti	Fe
Content	2.44	0.41	0.14	0.03	0.02	0.03	0.03	Balance

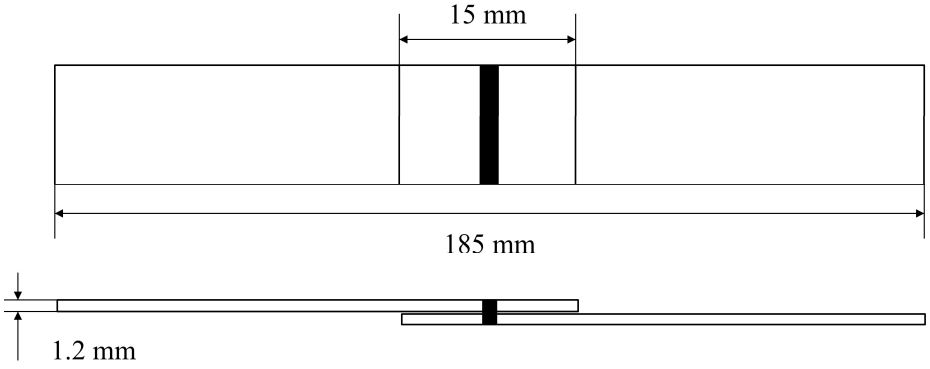


Figure 1. Geometry and dimensions of the laser-welded lap-joint specimen.

Laser-welding experiments were conducted using an HCFM-6000 fiber-laser system with a nominal wavelength of 1070 nm and an adjustable spot-diameter range of 0.2–0.6 mm. High-purity argon (99.99%) was supplied as the shielding gas at a flow rate of 15–20 L min^{-1}. The laser beam was oriented perpendicular to the rolling direction of the steel sheets. Preliminary welding trials were used to define the investigated process window. The ranges of laser power, welding speed, defocusing distance, and shielding-gas flow rate are listed in Table 2.

Table 2. Investigated laser-welding process parameters and ranges.

Process parameter	Range
Laser power	3400–4300 W
Welding speed	30–39 mm/s
Defocusing distance	–0.3 to 0.3 mm
Shielding gas flow rate	15–20 L/min

Metallographic specimens were sectioned from the central region of the weld seam. The specimens were ground sequentially using 500–2000-grit abrasive papers, mechanically polished with an alumina suspension, and etched in a 4% nitric acid–alcohol solution. Weld microstructures and grain

morphologies were examined at 200× magnification using a KEYENCE VHX-7000 three-dimensional optical microscope. The resulting metallographic images provided experimental references for morphology-level assessment of the CA predictions. Figure 2 shows the mounted cross-sectional specimens and the optical-microscopy system.

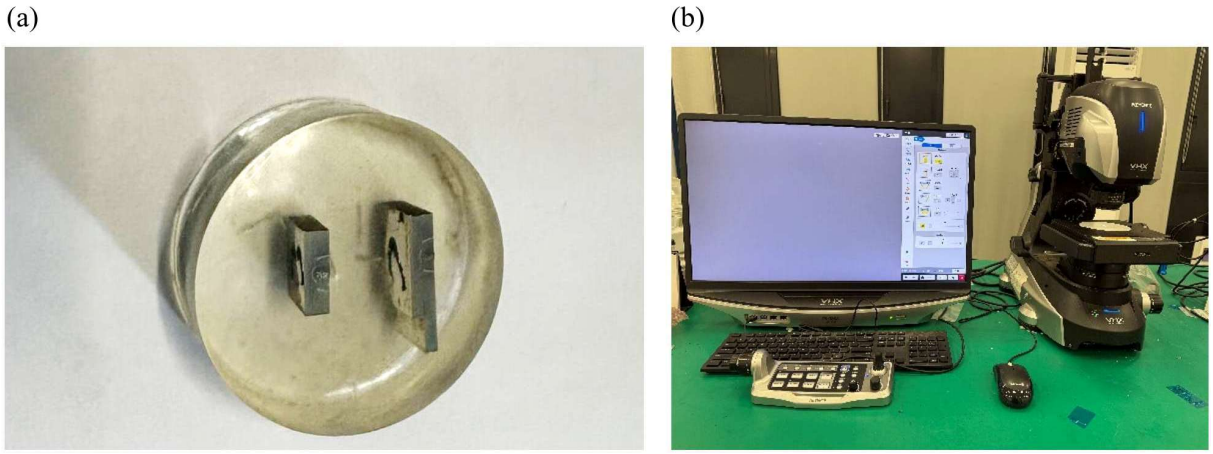


Figure 2. Metallographic characterization. (a) Mounted weld cross-sectional specimens; (b) KEYENCE VHX-7000 optical-microscopy system.

The welding experiments and metallographic characterization provided the experimental basis for the numerical analysis. The observed weld morphology informed the geometric interpretation of the simulated fusion region, while the metallographic observations provided reference morphologies for assessing the CA results. The investigated welding parameters also defined the input domain of the thermophysical FE simulations and the subsequent CNN–LSTM surrogate model.

2.2. Thermophysical finite element simulation

A three-dimensional thermophysical FE model was developed in ABAQUS to calculate the transient temperature field during laser welding of QP1180 steel. The model reproduced the lap-joint geometry described in Section 2.1 and had overall dimensions of 185 × 100 × 2.4 mm, comprising two 1.2-mm-thick sheets with a 15-mm overlap. The calculated thermal histories at the weld-center cross-section were subsequently used to derive the cooling-rate fields for CNN–LSTM training. Figure 3 shows the model geometry and mesh.

A non-uniform mesh was used to resolve the steep temperature gradients near the weld seam while limiting the overall computational cost. The weld seam and adjacent HAZ were locally refined using a nominal element size of 0.1 × 0.1 × 0.3 mm. The element size was gradually increased with distance from the refined region. The model was discretized using eight-node coupled temperature–displacement brick elements with trilinear displacement and temperature interpolation (C3D8RT).

Temperature-dependent density, thermal conductivity, and specific heat capacity were calculated for QP1180 steel using JMatPro 7.0 based on the nominal chemical composition. The calculated values were entered into ABAQUS as tabulated material data over the temperature range of 20–1600 °C. Phase change was represented by specifying a latent heat of 3.00×10^5 J kg^{-1} over the solidus–liquidus interval of 1471.43–1507.56 °C. This treatment accounts for the additional energy absorbed during

melting. Table 3 reports representative ranges of the temperature-dependent properties together with the phase-change parameters; the listed ranges should not be interpreted as temperature-independent constants.

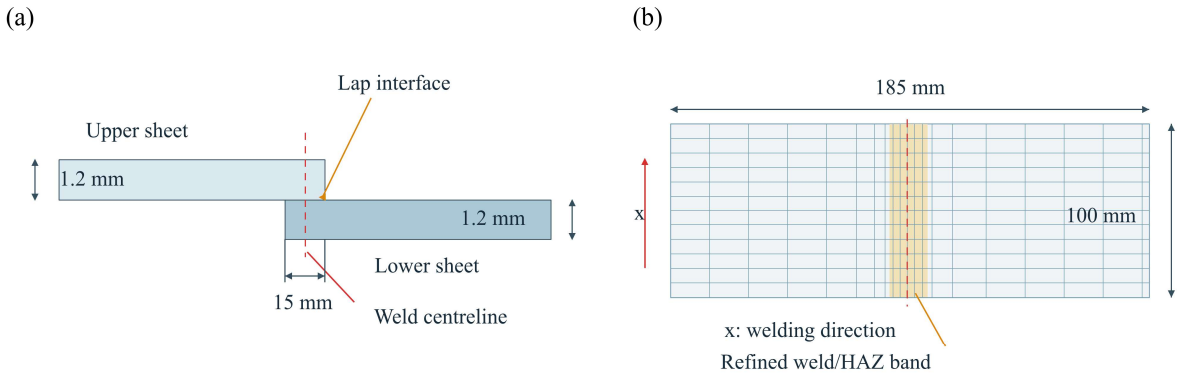


Figure 3. FE model geometry and mesh layout. (a) Lap-joint geometry; (b) overall mesh layout.

Table 3. Representative material-property ranges and phase-change parameters used in the FE simulation.

Parameter	Value
Thermal conductivity (λ)	25~40 W/(m·K)
Density (ρ)	7400~7850 kg/m^3
Specific heat capacity (C_p)	450~650 J/(kg·K)
Modulus of elasticity (E)	200 GPa
Solidus temperature (Ts)	1471.43 ℃
Liquidus temperature (T_L)	1507.56 ℃
Latent heat (L)	3.00 × 10^5 J/kg

Convective and radiative heat losses were imposed on all exposed surfaces, including the upper and lower sheet surfaces and the lateral boundaries. The outward convective heat flux density was calculated using Newton's law of cooling, as expressed in Eq 1:

$$q_c = h(T - T_{\mathrm{env}}) \tag{1}$$

where q_c is the outward convective heat flux density, h is the convective heat transfer coefficient, T is the surface temperature, and T_{env} is the ambient temperature. The outward radiative heat flux density was calculated using the Stefan–Boltzmann law, as expressed in Eq 2:

$$q_{\mathrm{rad}} = \varepsilon\sigma(T^4 - T_{\mathrm{env}}^4) \tag{2}$$

where q_{rad} is the outward radiative heat flux density, ε is the surface emissivity, and σ is the Stefan–Boltzmann constant. In Eq 2, T and T_{env} are absolute temperatures expressed in kelvin, whereas the temperature difference in Eq 1 can be expressed in either degrees Celsius or kelvin. Table 4 lists the boundary-condition parameters.

Table 4. Boundary condition parameters used in the FE simulation.

Parameter	Value
Convective heat transfer coefficient (h)	20 W m^{-2} K^{-1}
Radiative emissivity (ε)	0.6
Ambient temperature (T_{env})	25 ℃
Stefan–Boltzmann constant (σ)	5.67 × 10^{-8} W m^{-2} K^{-4}

The moving laser heat input was represented using Goldak's double-ellipsoid heat-source model [22], which accounts for the asymmetric energy distribution ahead of and behind the molten-pool center. The heat source was implemented in ABAQUS through the DFLUX user subroutine. The volumetric heat-generation rate in the front half-ellipsoid, where $x \geq x_n(t)$, was defined by Eq 3:

$$q_f = \frac{6\sqrt{3} f_f Q \eta}{a_f b c \pi \sqrt{\pi}} \exp\left[-3\left(\frac{[x - x_n(t)]^2}{a_f^2} + \frac{y^2}{b^2} + \frac{z^2}{c^2}\right)\right] \tag{3}$$

The volumetric heat-generation rate in the rear half-ellipsoid, where $x < x_n(t)$, was defined by Eq 4:

$$q_r = \frac{6\sqrt{3} f_r Q \eta}{a_r b c \pi \sqrt{\pi}} \exp\left[-3\left(\frac{[x - x_n(t)]^2}{a_r^2} + \frac{y^2}{b^2} + \frac{z^2}{c^2}\right)\right] \tag{4}$$

where q_f and q_r are the volumetric heat-generation rates in the front and rear half-ellipsoids, respectively, expressed in W m^{-3}. A local moving coordinate system was used for the heat source, with the x-axis aligned with the welding direction, the y-axis aligned with the transverse direction of the sheet, and the z-axis aligned with the thickness direction. The coordinate $x_n(t)$ denotes the position of the heat-source center along the welding direction at time t. The parameters a_f and a_r are the front and rear semi-axis lengths in the welding direction, respectively, while b and c are the transverse and through-thickness semi-axis lengths. All coordinates and semi-axis lengths are expressed in meters. Here, Q is the laser power, η is the laser absorption efficiency, and f_f and f_r are the front and rear energy-distribution coefficients, respectively, with $f_\mathrm{f} + f_\mathrm{r} = 2$. Figure 4 illustrates the double-ellipsoid heat-source model.

The heat-source center was updated at each time increment according to $x_n(t) = x_0 + vt$, where x_0 is the initial position and v is the welding speed. At each integration point, the DFLUX subroutine evaluated the relative coordinate $x - x_n(t)$. The front heat-source expression was applied when $x - x_n(t) \geq 0$, whereas the rear expression was applied when $x - x_n(t) < 0$.

Table 5 summarizes the calibrated parameters of the double-ellipsoid heat-source model. The geometric parameters and energy-distribution coefficients were determined by comparing the simulated fusion-zone geometry with the experimental weld cross-sections. The absorption efficiency was adjusted together with the surface emissivity and convective heat-transfer coefficient to reproduce the measured local temperature–time history.

The calibrated values constitute a common heat-source parameter set for the investigated process window. The available calibration data comprised one local experimental temperature history and did not include repeated or co-located multipoint measurements. A formal uncertainty-propagation or global sensitivity analysis was therefore not performed. The transferability of the calibrated parameter

set beyond the investigated material, joint geometry, and process window required additional experimental validation.

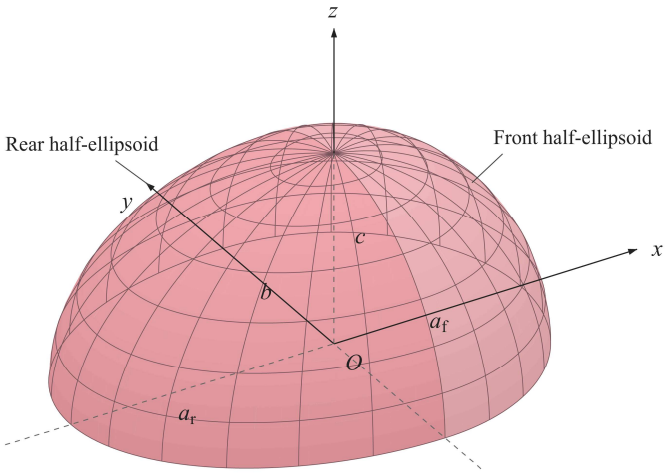


Figure 4. Schematic diagram of the double-ellipsoid heat source model.

Table 5. Calibrated parameters of the double-ellipsoid heat-source model.

Parameter	Symbol	Value	Determination basis
Laser absorption efficiency	η	0.70	Thermal-history calibration
Front semi-axis	a_f	3 mm	Fusion-zone geometry calibration
Rear semi-axis	a_r	6 mm	Fusion-zone geometry calibration
Transverse semi-axis	b	3 mm	Fusion-zone geometry calibration
Depth semi-axis	c	3 mm	Fusion-zone geometry calibration
Front energy-distribution coefficient	f_f	0.70	Fusion-zone geometry calibration
Rear energy-distribution coefficient	f_r	1.30	Fusion-zone geometry calibration

2.3. Cooling-rate dataset and CNN–LSTM surrogate model

The cooling-rate dataset was generated from thermal histories calculated using the calibrated FE model. Latin hypercube sampling was used to generate 300 combinations of laser power, welding speed, and defocusing distance within the investigated process window [23]. For each parameter combination, temperature histories were extracted from a 10 × 20 grid covering the fusion zone and adjacent HAZ at the weld-center cross-section. Cooling-rate magnitudes were calculated from the cooling portions of these histories and arranged into a 10 × 20 spatial matrix. Each matrix was subsequently flattened into a 200-dimensional target vector. The three process parameters and the cooling-rate targets were standardized separately using StandardScaler. The dataset was divided into training and held-out test subsets at a ratio of 8:2.

The final CNN–LSTM architecture comprised two one-dimensional convolutional layers, three stacked bidirectional LSTM layers, and a fully connected output layer. The input vector was defined as $x \in \mathrm{R}^{B\times 3}$, where B is the batch size and the three features are laser power, welding speed, and defocusing distance. A dimensional-expansion operation transformed the input into $X_{\mathrm{initial}} =$

$\mathrm{unsqueeze}(x) \in \mathrm{R}^{B\times 1\times 3}$ for one-dimensional convolution. Both convolutional layers used a kernel size of 3 and 128 output channels, followed by ReLU activation and max-pooling. The resulting feature tensor was permuted from (B, C_{cnn}, L) to (B, L, C_{cnn}) and supplied to the stacked bidirectional LSTM layers. Each LSTM layer contained 192 hidden units. The hidden representation at the final sequence position was mapped by a fully connected layer to a 200-dimensional vector and reshaped into the 10 × 20 cooling-rate field.

Because the three process inputs do not form a physical time sequence, the LSTM does not represent the temporal evolution of the measured temperature history. Instead, it models dependencies among the learned feature tokens produced by the convolutional layers. The CNN layers extract local relationships among the process variables, whereas the bidirectional LSTM aggregates dependencies among the resulting feature representations. The CNN–LSTM therefore functions as a learned feature-to-field surrogate: The calibrated FE model provides the physically based thermal histories, and the neural network learns the nonlinear mapping from process parameters to the spatial cooling-rate field [24,25].

Figure 5 illustrates the CNN–LSTM architecture, which comprises two one-dimensional convolutional layers, three stacked bidirectional LSTM layers, and a fully connected output layer.

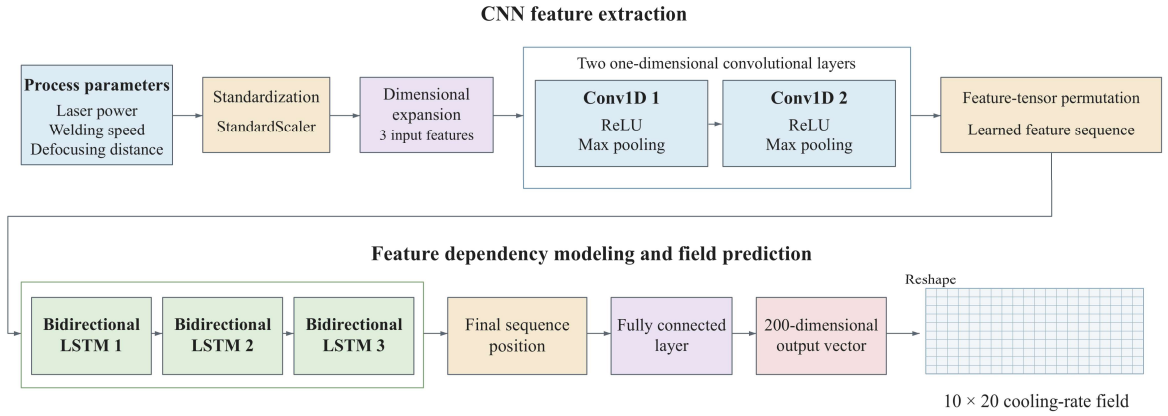


Figure 5. Architecture of the CNN–LSTM surrogate model for cooling-rate-field prediction.

The model was trained using the Smooth L1 loss with $\beta = 0.21$, a learning rate of 0.001 and a batch size of 64. Bayesian optimization combined with cross-validation was used to tune the principal hyperparameters, including the learning rate, LSTM hidden size, and number of convolutional output channels. To improve initialization, a shallow network containing two convolutional and pooling layers was first trained to learn basic feature representations. Model performance was evaluated using the mean absolute error (MAE), root mean square error (RMSE), and coefficient of determination (R^2).

Within the sampled process window, the trained CNN–LSTM model was used to estimate cooling-rate fields for new combinations of welding parameters. Compared with running a new FE simulation for every parameter combination, the surrogate provides a faster means of obtaining the cooling-rate distribution at the weld-center cross-section. The predicted field was subsequently supplied to the CA model as the thermal input for solidification-microstructure simulation.

2.4. Cellular automaton (CA) model for solidification microstructure prediction

A CA model was developed to simulate solidification-grain evolution in the laser-welded zone. The CNN–LSTM model predicts the cooling-rate magnitude C*i* at each point of the 10 × 20 weld-center grid. For each grid point, a local time coordinate τ was defined such that τ = 0 corresponds to the instant when the local temperature reaches the liquidus temperature. Assuming a constant cooling rate over the solidification interval, the local temperature history was reconstructed using Eq 5:

$$T_i(\tau) = T_l - C_i\tau, 0 \le \tau \le \Delta t_i \tag{5}$$

where $T_i(\tau)$ is the temperature at grid point i at local time τ, T_l = 1507.56 °C is the liquidus temperature, and Δt_i is the duration of the local solidification interval, calculated using Eq 6:

$$\Delta t_i = \frac{T_l - T_s}{C_i} \tag{6}$$

where T_s = 1471.43 °C is the solidus temperature. The reconstructed temperature histories were spatially interpolated from the 10 × 20 thermal grid onto the 500 × 500 μm CA domain using bicubic interpolation, with a CA cell size of 1 μm. The resulting temperature field was used to calculate local undercooling and drive the nucleation and grain-growth calculations. This linear reconstruction was applied only over the liquidus-to-solidus interval and does not represent the complete heating history or the post-solidification thermal cycle.

Bicubic interpolation transfers the reconstructed temperature histories from the 10 × 20 source grid to the CA lattice but does not add independent thermal information to the CNN–LSTM prediction. The CA cell size of 1 μm determines the numerical resolution for interface migration and grain competition, whereas the spatial resolution of the thermal driving field remains governed by the 10 × 20 source grid. Thermal variations below the source-grid spacing are therefore not independently resolved.

Nucleation was described using a continuous nucleation model [26]. The nucleation density was prescribed as a function of local undercooling, with separate parameter sets for the fusion-boundary region and the molten-pool interior. At the fusion boundary, the maximum nucleation undercooling was set to 3 K and the maximum nucleation density to 3×10^8 m^{-2}. In the molten-pool interior, the corresponding values were 10 K and 6×10^8 m^{-2}. These parameter sets represent heterogeneous nucleation near the fusion boundary and enhanced undercooling-driven nucleation in the molten-pool interior.

Solute redistribution and interface migration were described using the interface-cell growth-velocity relation presented below, with D_l = 5000 μm^2 s^{-1}, Ds = 1 μm^2 s^{-1}, and k_0 = 0.72. These CA parameters were applied as one common set throughout the investigated process window. They were not independently measured for each welding condition. The CA model was therefore used to compare spatial trends in solidification morphology under different thermal histories rather than to infer condition-specific material constants.

The reconstructed temperature field provides the thermal information relevant to solidification. The local temperature-gradient magnitude is defined as $G = |\nabla T|$. At the liquidus isotherm, the macroscopic solidification-front speed can be estimated using Eq 7:

$$V_s = \frac{|\partial T/\partial t|}{G} \tag{7}$$

where V_s is the macroscopic solidification-front speed, $|\partial T/\partial t|$ is the local cooling-rate magnitude, and G is the local temperature-gradient magnitude. Here, V_s corresponds to the solidification rate conventionally denoted by R in the G/R framework. Neither G nor V_s was introduced as an additional CNN–LSTM output or an independently fitted CA parameter. Their effects are inherited from the reconstructed spatiotemporal temperature field: the local heat-flow direction is opposite to the temperature gradient, while the CA interface advances according to the local undercooling-dependent growth kinetics. Accordingly, G/V_s is interpreted as a qualitative descriptor of the simulated grain morphology rather than as an independently calibrated model output. A relatively large G/V_s favors directional columnar growth, whereas a smaller value increases the tendency toward equiaxed growth.

Grain growth was calculated based on solute diffusion and interface migration. The normal growth velocity of an interface cell was calculated using Eq 8:

$$V_n = \frac{D_l(1 - C_l^*/C_l)}{(1 - k_0)d_x} + \frac{k_0 D_s \left(1 - \frac{C_s^*}{k_0 C_l^*}\right)}{(1 - k_0)d_x} \tag{8}$$

where V_n is the normal growth velocity of the interface cell, D_l and D_s are the solute diffusion coefficients in the liquid and solid phases, respectively, C_l^* and C_l are the equilibrium and local solute concentrations in the liquid phase, respectively, C_s^* is the equilibrium solute concentration in the solid phase, k_0 is the equilibrium partition coefficient, and d_x is the cell size. The solid fraction of the interface cell was updated using Eq 9:

$$f_s^{t+\Delta t} = f_s^t + \frac{V_n \Delta t}{L_\phi} \tag{9}$$

where f_s^t and $f_s^{t+\Delta t}$ are the solid fractions before and after the time increment, respectively, Δt is the time step, and L_ϕ is the interface stability length.

The CA simulation produced the spatial distribution of grains and crystallographic orientations in the weld cross-section. Different colors represent different crystallographic orientations and are used to visualize columnar and equiaxed grain formation. The simulated microstructure was compared with the metallographic observations described in Section 2.1. This comparison assessed whether the CA model reproduced the principal solidification features of laser-welded QP1180 steel, particularly columnar growth near the fusion boundary and equiaxed-grain formation near the weld center. The expected transition in solidification morphology is illustrated in Figure 6.

Based on the above procedure, the complete prediction framework consisted of four sequential steps: laser welding experiments and metallographic characterization, thermophysical FE simulation, CNN–LSTM cooling-rate prediction, and CA microstructure simulation. The experimental results were used to calibrate and validate the numerical models. The calibrated FE model provided physically based cooling-rate data for training the CNN–LSTM surrogate model, and the predicted cooling-rate fields were then used to drive the CA simulation. This workflow linked process parameters with thermal response and microstructure evolution, providing the methodological basis for the results and discussion in the following sections.

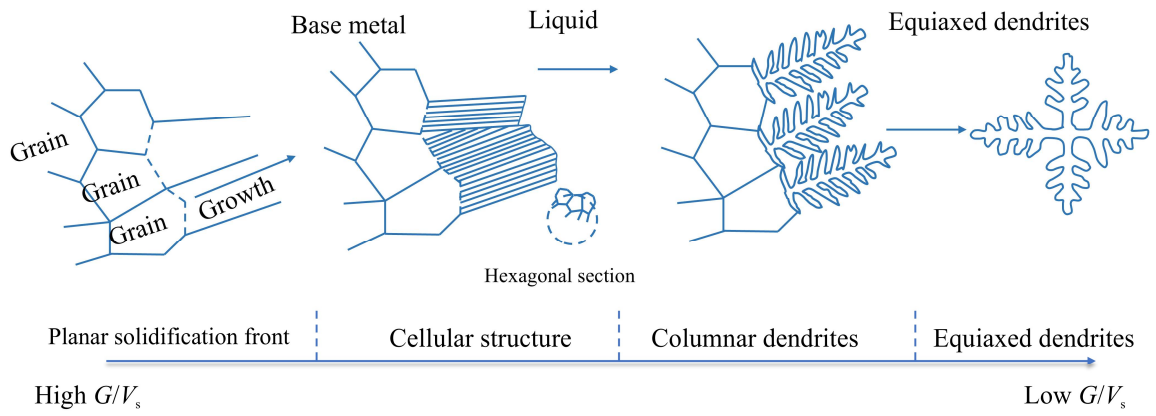


Figure 6. Schematic diagram of grain nucleation and growth in the cellular automata model.

3. Results and discussion

3.1. Experimental weld morphology and microstructure

The experimental weld morphology and microstructure were characterized to establish the experimental basis for the numerical analysis. Metallographic specimens were sectioned from the central cross-section of the weld seam and examined after grinding, polishing, and chemical etching. The observations confirmed the formation of a localized fusion region and thermally affected microstructural changes in the welded joint. These observations were used as reference information for interpreting the thermophysical FE model and assessing the subsequent CA simulation.

3.2. Validation of the thermophysical finite element model

The thermophysical FE model was calibrated using a thermocouple temperature–time curve measured near the weld seam. The thermocouple junction was spot-welded to the upper surface of the top sheet at a transverse distance of 3.0 mm from the weld centerline. The simulated thermal history was extracted from the FE node corresponding to the same geometric position.

Figure 7a shows the temperature-acquisition arrangement, including the thermocouple positioned near the weld seam and the corresponding sampling node in the FE model. The transverse offset of the thermocouple was measured before welding, and the same spatial coordinate was used to extract the corresponding FE temperature history. Figure 7b compares the measured and simulated temperature–time curves at this calibration location. Both curves reached peak temperatures of approximately 470 °C. The relative peak-temperature difference was calculated as $\left|T_{\mathrm{p,FE}} - T_{\mathrm{p,exp}}\right|/T_{\mathrm{p,exp}} \times 100\%$, where $T_{\mathrm{p,FE}}$ and $T_{\mathrm{p,exp}}$ are the peak temperatures extracted from the numerical data of the simulated and experimental curves, respectively. The resulting peak-temperature difference was below 5%. Similarly, the relative cooling-rate difference was calculated as $\left|R_{\mathrm{FE}} - R_{\mathrm{exp}}\right|/R_{\mathrm{exp}} \times 100\%$, using the cooling-rate values extracted from the corresponding cooling portions of the two curves, and was below 10%.

These results demonstrate agreement in the local heating and cooling behavior at the calibration location. However, because the measured peak temperature was below the liquidus temperature of QP1180 steel, this comparison does not directly validate the fusion-zone temperature.

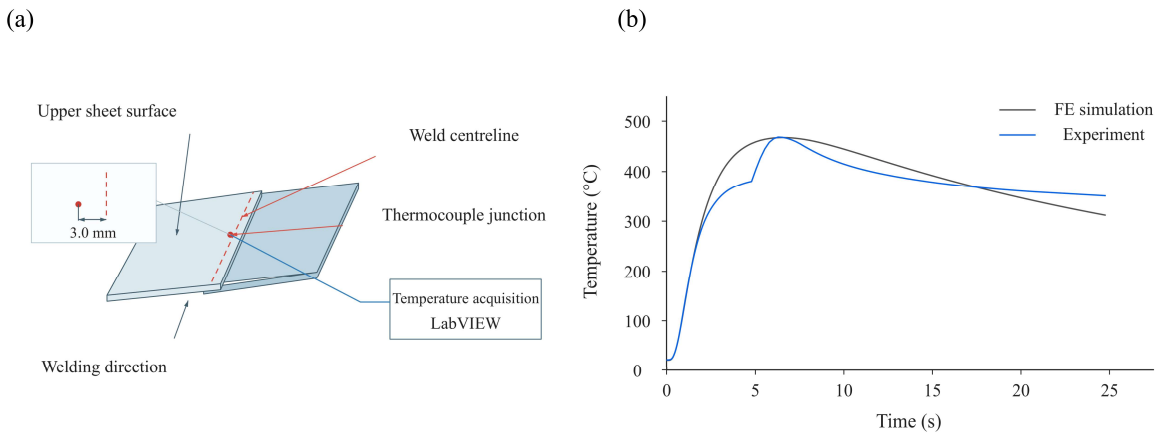


Figure 7. Local thermal-history calibration of the FE model. (a) Thermocouple placement; (b) comparison between the simulated and measured temperature histories.

Figure 8 shows the calculated temperature distribution at the weld-center cross-section, with selected temperature levels labelled. The results illustrate the localized high-temperature region and the decrease in temperature toward the surrounding material. Figure 7 presents the local thermal-history calibration, whereas Figure 8 illustrates the simulated cross-sectional temperature distribution.

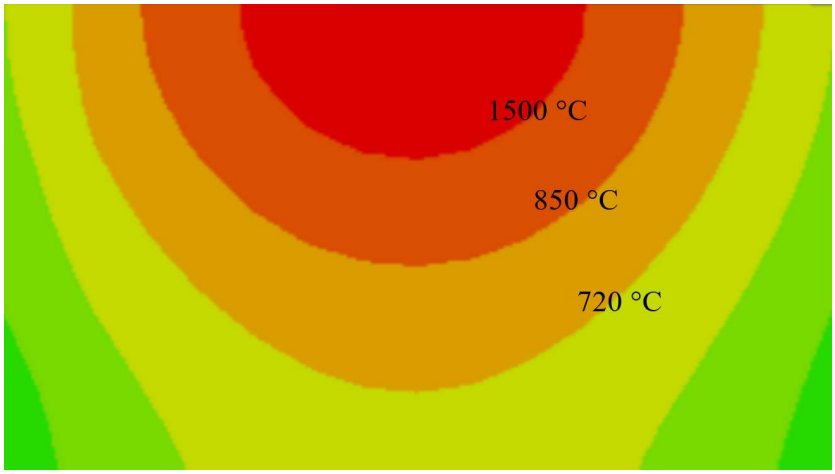


Figure 8. Calculated cross-sectional temperature field of the QP1180 steel laser-welded joint.

The calibrated FE model was subsequently used to extract temperature histories from the 10 × 20 grid at the weld-center cross-section, covering the fusion zone and the adjacent HAZ. During cooling, the local cooling-rate magnitude was calculated from two consecutive temperature–time data points using Eq 10:

$$R_i = -\frac{T_{i+1} - T_i}{t_{i+1} - t_i} \tag{10}$$

where T_i and T_{i+1} are the calculated temperatures at times t_i and t_{i+1}, respectively. The negative sign gives a positive cooling-rate magnitude when the temperature decreases. The resulting values were organized into a 10 × 20 spatial matrix and used as the target field for the CNN–LSTM model.

The cooling-rate difference below 10% reported in Figure 7 was calculated from the measured and simulated thermal histories at the thermocouple location. In contrast, the spatial cooling-rate field in the fusion zone and adjacent HAZ was calculated from the calibrated FE temperature histories and was not obtained from direct multipoint experimental measurements.

3.3. Cooling-rate prediction by the CNN–LSTM model

The CNN–LSTM model was evaluated using the FE-derived dataset described in Section 2.3. Laser power, welding speed, and defocusing distance served as the input variables, while the cooling-rate distribution over the 10 × 20 grid at the weld-centre cross-section served as the prediction target. The dataset comprised 300 process-parameter combinations generated by Latin hypercube sampling within the investigated process window. Each cooling-rate matrix was flattened into a 200-dimensional target vector for model training and evaluation.

The CNN–LSTM model was trained to learn the nonlinear mapping from the normalized process parameters to the normalized cooling-rate field. Model performance on the held-out test set was evaluated using MAE, RMSE, and R^2, as defined in Eqs 11–13:

$$\mathrm{MAE} = \frac{1}{n}\sum_{i=1}^{n}|\hat{y}_i - y_i| \tag{11}$$

$$\mathrm{RMSE} = \sqrt{\frac{1}{n}\sum_{i=1}^{n}(\hat{y}_i - y_i)^2} \tag{12}$$

$$R^2 = 1 - \frac{\sum_{i=1}^{n}(y_i - \hat{y}_i)^2}{\sum_{i=1}^{n}(y_i - \bar{y})^2} \tag{13}$$

where y_i, $\hat{y}_i$, and $\bar{y}$ denote the FE-derived value, the CNN–LSTM prediction, and the mean FE-derived value, respectively, and n is the number of evaluated output elements. MAE and RMSE have the same units as the cooling-rate target, whereas R^2 is dimensionless.

Figure 9 presents the pointwise comparison between the CNN–LSTM predictions and the corresponding FE-derived cooling-rate values for the held-out test data. The signed residual for each output element was defined as $e_i = \hat{y}_i - y_i$. Accordingly, the vertical deviation from the identity line, $\hat{y} = y$, represents the pointwise prediction residual. The dashed lines indicate ±5% relative-error bounds and are included only as reference limits for pointwise agreement; they are not statistical confidence intervals. The global test-set metrics are summarized in Table 6.

Table 6 compares the CNN–LSTM model with standalone CNN and LSTM models evaluated using the same 200-dimensional target representation, fixed 8:2 data split, and performance metrics. The CNN–LSTM model achieved a higher R^2 and lower MAE and RMSE than either standalone model under this evaluation split. Specifically, R^2 increased from 0.80 for CNN and 0.74 for LSTM to 0.88 for CNN–LSTM, while MAE and RMSE decreased to 0.25 and 0.38, respectively. In the hybrid architecture, the CNN extracts local relationships from the process-parameter representation, while the LSTM aggregates dependencies among the learned feature tokens before generation of

the 200-dimensional cooling-rate field. These values represent a baseline comparison under one fixed data split and should not be interpreted as evidence of statistically significant superiority.

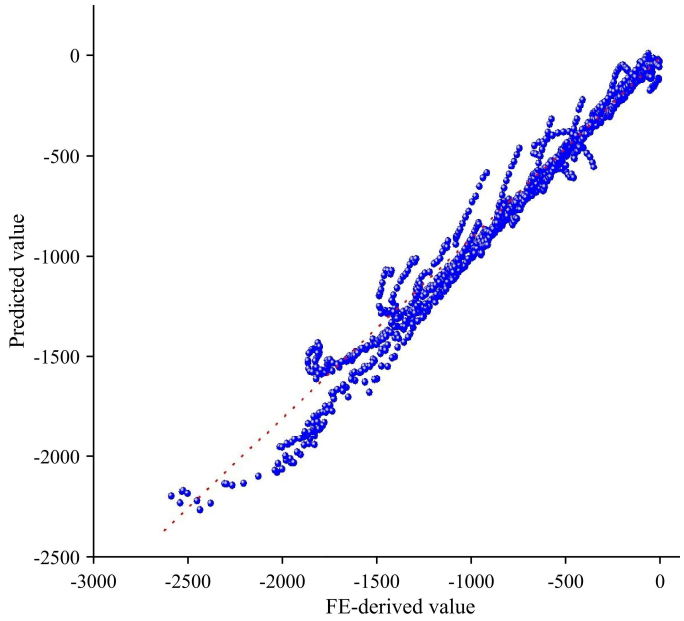


Figure 9. Comparison between predicted and FE-derived cooling-rate values obtained by the CNN–LSTM model.

Table 6. Held-out test-set performance of the cooling-rate surrogate models.

Model type	R^2	MAE	RMSE
CNN	0.80	0.31	0.44
LSTM	0.74	0.41	0.63
CNN–LSTM	0.88	0.25	0.38

Note: MAE and RMSE are reported in the units of the cooling-rate target, whereas R^2 is dimensionless. The metrics were calculated over the 200 output elements for the held-out test set.

The trained CNN–LSTM surrogate generated the cooling-rate field required for the subsequent CA calculation without rerunning the complete FE analysis for every candidate parameter combination. This establishes the connection between the welding parameters and the thermal input to the grain-scale solidification model. Because no systematic wall-clock benchmark was performed, the computational benefit is interpreted qualitatively rather than as a quantified acceleration ratio.

3.4. Cellular automata prediction of weld microstructure

The CNN–LSTM-predicted cooling-rate fields were converted into local temperature–time histories over the solidification interval using the procedure described in Section 2.4. These histories were interpolated from the 10 × 20 source grid onto the 500 × 500 μm CA domain and used to calculate the local undercooling that drives nucleation and grain growth. The CNN–LSTM output therefore provides a reduced thermal representation for the CA calculation rather than a reconstruction of the

complete transient FE temperature field. The CA output represents the solidification-grain morphology and crystallographic-orientation field generated during the liquid-to-solid transition. It does not represent the final multiphase microstructure produced by subsequent solid-state transformations in QP1180 steel.

Figure 10 compares the CA-predicted solidification-grain morphology with the experimentally observed post-welding microstructure. In the CA result, different colors denote different crystallographic orientations, whereas the metallographic image contains the effects of solidification and subsequent solid-state transformations. The comparison therefore focuses on the spatial morphology trend: directional columnar growth near the fusion boundary and a progressively more equiaxed region toward the weld center. It should be interpreted as a morphology-level comparison rather than as a one-to-one correspondence between simulated solidification grains and final metallographic grains.

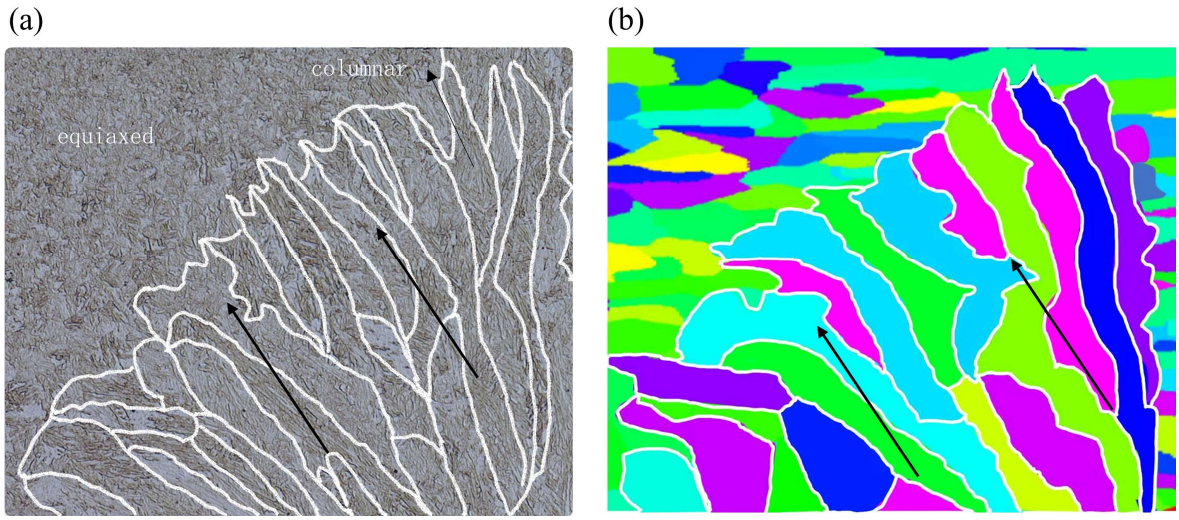


Figure 10. Morphology-level comparison between (a) the experimentally observed post-welding microstructure and (b) the CA-predicted solidification-grain morphology at the weld cross-section.

The simulation reproduced the principal spatial trend observed in the weld cross-section, namely columnar growth near the fusion boundary and a more equiaxed morphology toward the weld center. Near the fusion boundary, a large temperature gradient establishes a preferred heat-flow direction and promotes epitaxial columnar growth. Toward the weld center, the temperature gradient decreases, while increased local undercooling promotes the formation of equiaxed grains and restricts the continued inward growth of columnar grains. In the CA model, the solidification-front velocity V_S is governed by the local interface-growth kinetics and the undercooling-dependent growth law; it is not an additional CNN–LSTM output. The conventional G/R framework is represented here by G/V_S. A relatively large G/V_S favors directional columnar growth, whereas a smaller value is associated with an increased tendency for the columnar-to-equiaxed transition. Because an independently calibrated G/V_S field was not generated, this interpretation remains qualitative.

Laser-welding studies have similarly shown that temperature gradients, cooling conditions, and external control of molten-pool behavior affect grain morphology. Guo et al. reported that ultrasonic

vibration reduced the local temperature gradient and promoted the columnar-to-equiaxed transition in Ti6Al4V laser welding [27]. Liu et al. showed that synchronous gas cooling altered the thermal history and cooling rate, resulting in grain refinement [28]. Zhao et al. combined thermal simulation with experimental characterization to relate asymmetric temperature-gradient distributions to columnar and equiaxed grain evolution in dissimilar aluminium-alloy laser welding [29]. These studies support the use of thermal-gradient and cooling-history information to interpret spatial variations in weld grain morphology.

The Figure 10 comparison should not be interpreted as statistical validation of grain-scale metrics across the complete process window. Quantitative validation of grain size, columnar-grain fraction, columnar-to-equiaxed transition position, and crystallographic-orientation distribution was not performed across welding conditions. Figure 10 therefore assesses only the overall morphology-level correspondence between the CA prediction and the experimental observation.

The coupled framework links the welding parameters to the predicted solidification morphology through an explicitly defined thermal pathway. The calibrated FE model supplies the thermal histories used to generate the training data, the CNN–LSTM surrogate predicts the spatial cooling-rate field, and the CA model converts the reconstructed solidification histories into grain morphology. Within the calibrated domain, this workflow reduces the need to repeat the complete FE calculation for every candidate condition while retaining a physical connection between process parameters, thermal response, and solidification behavior.

The applicability of the framework is limited to the investigated QP1180 steel grade, sheet thickness, lap-joint geometry, laser-welding configuration, and process-parameter window. The CNN–LSTM surrogate is intended for interpolation within the FE-generated training domain; its extrapolation to different materials, thicknesses, joint configurations, or substantially different process conditions has not been established. In addition, the CA model predicts solidification-grain morphology rather than the final multiphase microstructure after subsequent solid-state transformations. Mechanical properties, porosity, cracking, and other weld defects were not independently validated. The framework should therefore be used for candidate-condition comparison within the calibrated domain rather than as a substitute for experimental validation or high-fidelity FE analysis outside that domain.

4. Conclusions

In this study, we developed an FE-informed CNN–LSTM and CA framework that links welding parameters to cooling-rate fields and solidification-grain morphology in laser-welded QP1180 steel. The main conclusions are as follows:

(1) A three-dimensional thermophysical FE model was calibrated against a local thermocouple temperature history. At the calibration location, the selected peak-temperature and cooling-rate differences were below 5% and 10%, respectively. These values represent local calibration metrics and do not constitute direct experimental validation of the fusion-zone temperature. The calibrated FE model was subsequently used to generate the thermal histories required for cooling-rate-field construction.

(2) The CNN–LSTM surrogate mapped laser power, welding speed, and defocusing distance to a 200-dimensional cooling-rate field extracted from a 10 × 20 grid at the weld-center cross-section. On the fixed held-out test set, the model achieved $R^2 = 0.88$, MAE = 0.25, and RMSE = 0.38. It yielded a higher R^2 and lower MAE and RMSE than the standalone CNN and LSTM models under the same evaluation split.

(3) The predicted cooling-rate fields were converted into approximate local temperature histories over the solidification interval and supplied to the two-dimensional CA model. The resulting morphology reproduced the qualitative transition from directional columnar growth near the fusion boundary to a more equiaxed region toward the weld center. This comparison supports assessment of the overall spatial morphology trend; it does not establish quantitative accuracy for grain size, columnar-grain fraction, transition position, or crystallographic orientation.

(4) The coupled framework avoids rerunning the complete FE analysis for every candidate parameter combination while retaining an explicit connection between the welding parameters, thermal response, and solidification morphology. Because wall-clock time and hardware-dependent acceleration were not systematically benchmarked, the computational benefit is interpreted qualitatively rather than as a verified speed-up ratio.

(5) The applicability of the framework is limited to the investigated QP1180 steel grade, sheet thickness, lap-joint geometry, laser-welding configuration, and process-parameter window. The CNN–LSTM surrogate is intended for interpolation within the FE-generated training domain. The CA model describes solidification-grain morphology rather than the final multiphase microstructure after subsequent solid-state transformations. Mechanical properties, porosity, cracking, and other weld defects were not independently validated. The framework should therefore be used for candidate-condition comparison within the calibrated domain rather than as a substitute for experimental validation or high-fidelity FE analysis outside that domain.

Use of AI tools declaration

Generative AI tools were used solely to assist with English-language editing and text organization during manuscript revision. All scientific content, numerical results, interpretations and final wording were reviewed and approved by the authors.

Acknowledgments

The authors gratefully acknowledge the financial support from Chongqing Wanfeng Aowei Aluminum Wheel Co., Ltd. (Project No. FLKJ2026AAG2035). This work was also funded by the Chongqing Talent Program—Innovation and Entrepreneurship Demonstration Team (No. CQYC20220309977) and the Chongqing Special Major Project on Science and Technology Innovation and Application Development (No. CSTB2023YIAD-STX0024).

Author contributions

Xiaojuan Li: conceptualization, methodology, writing–original draft, writing–review & editing; Zhenfei Zhan: conceptualization, supervision, funding acquisition, writing–review & editing; Liangjun Zhang: resources, project administration; Silong Zhou: resources, investigation; Zhong Liao: resources, validation; Huayang Xiang: methodology, investigation, software, formal analysis, validation, visualization; Yuxiang Ji: formal analysis, visualization, writing–review & editing; Fuhao Fan: investigation, data curation, validation. All authors have read and approved the final version of the manuscript.

Conflict of interest

The authors declare no conflict of interest.

References

1. Guo W, Wan Z, Peng P, et al. (2018) Microstructure and mechanical properties of fiber laser welded QP980 steel. *J Mater Process Technol* 256: 229–238. https://doi.org/10.1016/j.jmatprotec.2018.02.015
2. Xue J, Guo W, Zhang Y, et al. (2022) Local microstructure and mechanical characteristics of HAZ and tensile behavior of laser welded QP980 joints. *Mater Sci Eng A* 854: 143862. https://doi.org/10.1016/j.msea.2022.143862
3. Zhang W, Yang S, Lin Z, et al. (2020) Weld morphology and mechanical properties in laser spot welding of quenching and partitioning 980 steel. *J Manuf Process* 56: 1136–1145. https://doi.org/10.1016/j.jmapro.2020.05.057
4. Zhang W, Tao W, Yang S (2021) Mechanical properties and fracture behaviors in remote laser spot welding of quenching and partitioning 980 steel. *Opt Laser Technol* 140: 107053. https://doi.org/10.1016/j.optlastec.2021.107053
5. Mohammadi Zahrani M, Ranjbarnodeh E, Ketabchi M, et al. (2024) Microstructure evolution and mechanical properties of laser-welded joints of 1.2 GPa-class quenching and partitioning steel. *Opt Laser Technol* 170: 110257. https://doi.org/10.1016/j.optlastec.2023.110257
6. Wei HL, Mukherjee T, Zhang W, et al. (2021) Mechanistic models for additive manufacturing of metallic components. *Prog Mater Sci* 116: 100703. https://doi.org/10.1016/j.pmatsci.2020.100703
7. Herzog D, Seyda V, Wycisk E, et al. (2016) Additive manufacturing of metals. *Acta Mater* 117: 371–392. https://doi.org/10.1016/j.actamat.2016.07.019
8. Zhang J, Liou F, Seufzer W, et al. (2016) A coupled finite element cellular automaton model to predict thermal history and grain morphology of Ti-6Al-4V during direct metal deposition (DMD). *Addit Manuf* 11: 32–39. https://doi.org/10.1016/j.addma.2016.04.004
9. Lian Y, Gan Z, Yu C, et al. (2019) A cellular automaton finite volume method for microstructure evolution during additive manufacturing. *Mater Des* 169: 107672. https://doi.org/10.1016/j.matdes.2019.107672
10. Teferra K, Rowenhorst DJ (2021) Optimizing the cellular automata finite element model for additive manufacturing to simulate large microstructures. *Acta Mater* 213: 116930. https://doi.org/10.1016/j.actamat.2021.116930
11. Liu S, Shin YC (2020) Integrated 2D cellular automata-phase field modeling of solidification and microstructure evolution during additive manufacturing of Ti6Al4V. *Comput Mater Sci* 183: 109889. https://doi.org/10.1016/j.commatsci.2020.109889
12. Rolchigo M, Stump B, Belak J, et al. (2020) Sparse thermal data for cellular automata modeling of grain structure in additive manufacturing. *Modell Simul Mater Sci Eng* 28: 065003. https://doi.org/10.1088/1361-651X/ab9734
13. Xiong F, Lian Y, Li MJ, et al. (2023) An extended cellular automaton finite volume method for grain nucleation–growth–coarsening during the wire-based additive manufacturing process. *Addit Manuf* 76: 103782. https://doi.org/10.1016/j.addma.2023.103782

14. Yuan L, Fattebert JL, Sun C, et al. (2024) Uncovering grain and subgrain microstructure at the scale of additive manufacturing melt tracks with a scalable cellular automaton solidification model. *Addit Manuf* 92: 104401. https://doi.org/10.1016/j.addma.2024.104401
15. Ren K, Chew Y, Zhang YF, et al. (2020) Thermal field prediction for laser scanning paths in laser aided additive manufacturing by physics-based machine learning. *Comput Methods Appl Mech Eng* 362: 112734. https://doi.org/10.1016/j.cma.2019.112734
16. Karniadakis GE, Kevrekidis IG, Lu L, et al. (2021) Physics-informed machine learning. *Nat Rev Phys* 3: 422–440. https://doi.org/10.1038/s42254-021-00314-5
17. Zhu Q, Liu Z, Yan J (2021) Machine learning for metal additive manufacturing: Predicting temperature and melt pool fluid dynamics using physics-informed neural networks. *Comput Mech* 67: 619–635. https://doi.org/10.1007/s00466-020-01952-9
18. Gunasegaram DR, Murphy AB, Barnard A, et al. (2021) Towards developing multiscale-multiphysics models and their surrogates for digital twins of metal additive manufacturing. *Addit Manuf* 46: 102089. https://doi.org/10.1016/j.addma.2021.102089
19. Ghungrad S, Faegh M, Gould B, et al. (2023) Architecture-driven physics-informed deep learning for temperature prediction in laser powder bed fusion additive manufacturing with limited data. *J Manuf Sci Eng* 145: 081007. https://doi.org/10.1115/1.4062237
20. Chen J, Pierce J, Williams G, et al. (2024) Accelerating thermal simulations in additive manufacturing by training physics-informed neural networks with randomly synthesized data. *J Comput Inf Sci Eng* 24: 011004. https://doi.org/10.1115/1.4062852
21. Tang J, Scheel P, Mohebbi MS, et al. (2024) On the calibration of thermo-microstructural simulation models for laser powder bed fusion process: integrating physics-informed neural networks with cellular automata. *Addit Manuf* 96: 104574. https://doi.org/10.1016/j.addma.2024.104574
22. Goldak J, Chakravarti A, Bibby M (1984) A new finite element model for welding heat sources. *Metall Trans B* 15: 299–305. https://doi.org/10.1007/BF02667333
23. McKay MD, Beckman RJ, Conover WJ (1979) Comparison of three methods for selecting values of input variables in the analysis of output from a computer code. *Technometrics* 21: 239–245. https://doi.org/10.1080/00401706.1979.10489755
24. LeCun Y, Bengio Y, Hinton G (2015) Deep learning. *Nature* 521: 436–444. https://doi.org/10.1038/nature14539
25. Hochreiter S, Schmidhuber J (1997) Long short-term memory. *Neural Comput* 9: 1735–1780. https://doi.org/10.1162/neco.1997.9.8.1735
26. Thévoz P, Desbiolles JL, Rappaz M (1989) Modeling of equiaxed microstructure formation in casting. *Metall Trans A* 20: 311–322. https://doi.org/10.1007/BF02670257
27. Guo J, Wang J, Cheng L, et al. (2024) Unravelling the mechanism of columnar-to-equiaxed transition and grain refinement in ultrasonic vibration assisted laser welding of Ti6Al4V titanium alloy. *Ultrasonics* 141: 107342. https://doi.org/10.1016/j.ultras.2024.107342
28. Liu Y, Wang J, Yan T, et al. (2024) Effect of synchronous gas cooling method on microstructure and mechanical properties of laser welded joint for Ti6Al4V titanium alloy. *Mater Today Commun* 39: 108779. https://doi.org/10.1016/j.mtcomm.2024.108779

29. Zhao Y, Hao L, Liu R, et al. (2024) Unravelling asymmetrical microstructure evolution and tensile fracture mechanism in laser welding of dissimilar 2219/2195 aluminum alloys. *J Mater Res Technol* 31: 4041–4058. https://doi.org/10.1016/j.jmrt.2024.07.087



AIMS Press

© 2026 the Author(s), licensee AIMS Press. This is an open access article distributed under the terms of the Creative Commons Attribution License (http://creativecommons.org/licenses/by/4.0)